Sterling McBride,[1] Ricardo Burdisso, [2] and Corina Sandu[3]

Modeling Vibration-Induced Tire-Pavement Interaction Noise in the Mid-frequency Range

REFERENCE: McBride, S., Burdisso, R., and Sandu, C., **"Modeling Vibration-Induced Tire-Pavement Interaction Noise in the Mid-frequency Range,"** *Tire Science and Technology*, Vol. 48, No. 4, October–December 2020, pp. XX–XX.

ABSTRACT: Tire-pavement interaction noise (TPIN) is one of the main sources of exterior noise produced by vehicles traveling at greater than 50 kph. The dominant frequency content is typically within 500–1500 Hz. Structural tire vibrations are among the principal TPIN mechanisms. In this work, the structure of the tire is modeled and a new wave propagation solution to find its response is proposed. Multiple physical effects are accounted for in the formulation. In an effort to analyze the effects of curvature, a flat plate and a cylindrical shell model are presented. Orthotropic and nonuniform structural properties along the tire's transversal direction are included to account for differences between its sidewalls and belt. Finally, the effects of rotation and inflation pressure are also included in the formulation. Modeled frequency response functions are analyzed and validated. In addition, a new frequency-domain formulation is presented for the computation of input tread pattern contact forces. Finally, the rolling tire's normal surface velocity response is coupled with a boundary element model to demonstrate the radiated noise at the leading and trailing edge locations. These results are then compared with experimental data measured with an on-board sound intensity system.

KEY WORDS: tire vibrations, tire-pavement interaction noise, tread-pattern noise, infinite flat plate tire model, cylindrical shell tire model, wave propagation

Introduction

Tire-pavement interaction noise (TPIN) is the largest source of noise produced by vehicles traveling at speeds between 50 and 150 kph. It is dominant over power train noise and aerodynamic noise. Power train noise is typically produced by the engine, transmission, intake, and exhaust; therefore, it is significant only at low speeds. On the other hand, aerodynamic noise becomes important only at very high speeds, at greater than 150 kph [*1*]. The TPIN dominant spectral content is between 500 and 1500 Hz. For example, Fig. 1a shows the noise produced by different tires rolling on the same pavement. These results were obtained after performing a large experimental campaign using an onboard sound intensity system (OBSI), as shown in Fig. 1b. Further details on how these measurements were collected can be found in [*2–4*].

[1] Corresponding author. Virginia Tech, Department of Mechanical Engineering, 635 Prices Fork Road, 445 Goodwin Hall, Blacksburg, VA, 24060, USA. Email: sterling.mcbride@vt.edu

[2] Virginia Tech, Department of Mechanical Engineering, 635 Prices Fork Road, 445 Goodwin Hall, Blacksburg, VA, 24060, USA. Email: rburdiss@vt.edu

[3] Virginia Tech, Department of Mechanical Engineering, 635 Prices Fork Road, 445 Goodwin Hall, Blacksburg, VA, 24060, USA. Email: csandu@vt.edu

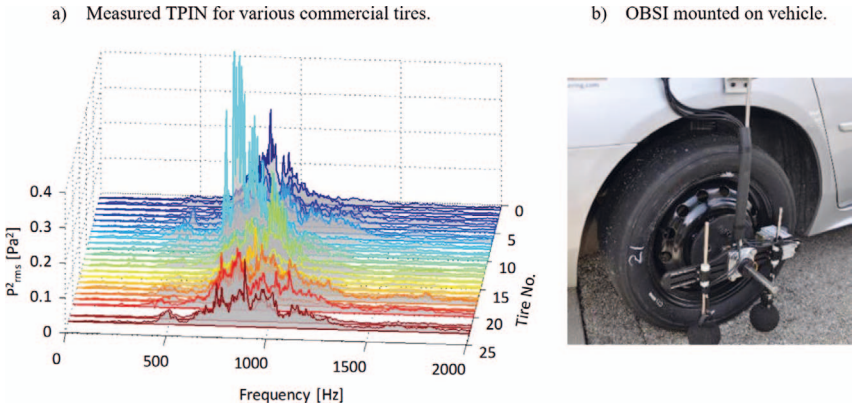

FIG. 1 — *(a) Measured TPIN for different tires. (b) Onboard sound intensity system used for testing.*

Modeling the mechanisms that produce TPIN behavior is an active research topic. Since the 1970s, the existence of multiple TPIN mechanisms has been speculated without any conclusive proof. Nevertheless, the noise produced by the vibratory response of the tire is a well-established mechanism and is addressed in this work.

In an effort to observe how noise behaves around a rolling tire, Donavan and Oswald [*5*] measured the sound intensity levels around a tire mounted on a vehicle while rolling. In this case, the highest noise levels were produced near the contact region and decayed along the circumferential direction of the tire. These results suggested that the tire is excited in the contact patch region, where waves that travel along its circumferential direction are excited and in turn generate the noise measured by the sound intensity probes. Additional insight on a tire's structural response was provided by Bernhard [*6*]. In this work, the response of the tire was measured with a laser Doppler vibrometer over a surface grid on the belt surface of the tire. The tire was excited using a dynamic shaker at a single point located at the center of the belt. These results showed that modes are observed along both directions of the tire for low frequencies. However, for higher frequencies (greater than 500 Hz), resonant behavior was no longer observed along the circumferential direction of the tire. In this case, propagating and decaying waves were observed.

Most approaches intended to model vibration-induced TPIN within the mid-frequency range are based on the modal expansion of the tire's response. Still, many researchers acknowledge the existence of waves along the circumferential direction of the tire, and many efforts have been directed toward such formulation without significant success (see, for example, the work presented by Kropp [*7*], O'Boy and Dowling [*8*], and Hoever [*9*]). Thus, innovative developments are still necessary to predict tire vibrations and noise

for higher frequencies with improved accuracy. In this work, the development of a structural model and a new approach to computing the response of a tire is presented. The main goal is to provide a physically based model suitable for predicting the vibratory response of the tire in the dominant mid-frequency range (500–1500 Hz). This is then coupled with the noise produced by implementing a boundary element method (BEM) code. Finally, measured and modeled tread pattern noise results are compared.

Modeling the Structure of a Tire

To model the tire's structural dynamic behavior, two approaches are explored. First, the tire is modeled as a flat plate that is infinite along the circumferential direction. Second, the tire is modeled as a cylindrical shell. The latter was developed in an effort to include curvature effects. Additional physical effects included in both approaches are the following:

1. Orthotropic material properties
2. Nonuniform properties along the transversal direction of the tire that account for structural differences between the tire's belt and sidewalls
3. Additional membrane tension terms that account for inflation pressure
4. Effects of rotation in the tire's structural dynamic behavior

This section presents the equations of motion for the infinite flat plate and the cylindrical shell models, including all the added terms that account for the physical effects listed above.

Infinite Flat Plate

The initial approach consists of modeling the tire as a simply supported plate that is infinite along its circumferential direction, as shown in Fig. 2. A smear representation of the actual tread pattern of the tire is implemented in this model. This allows assigning different masses and stiffnesses associated with the belt (including the smeared tread pattern) and the sidewalls.

Assuming that the plate is excited at the coordinate's system origin, waves traveling in the positive and negative x-direction do not interact with each other. Therefore, standing waves (i.e., modes) are not formed. This is the expected response of a tire in the mid-frequency range.

The equation of motion of the plate is defined as follows

$$-T_{0x}\frac{\partial^2 w}{\partial x^2} - T_{0y}\frac{\partial^2 w}{\partial y^2} + \left(\frac{\partial^2}{\partial y^2}\left(B_y(y)\frac{\partial^2 w}{\partial y^2}\right) + 2B_{xy}\frac{\partial^4 w}{\partial y^2 \partial x^2} + B_x\frac{\partial^4 w}{\partial x^4}\right)$$
$$-m(y)\frac{\partial^2 w}{\partial t^2} + m(y)\left(V_p^2\frac{\partial^2 w}{\partial x^2} + 2V_p\frac{\partial^2 w}{\partial x \partial t}\right) = f(t)\delta(x - x_f)\delta(y - y_f) \quad (1)$$

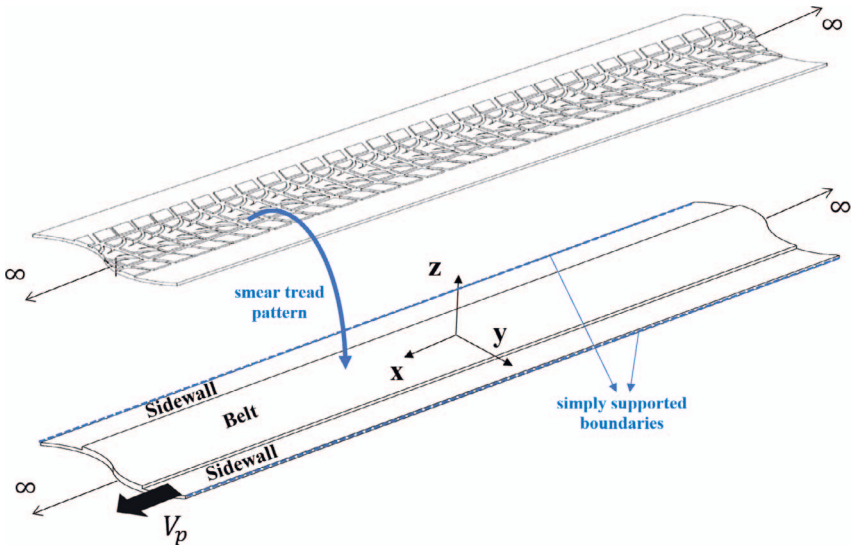

FIG. 2 — *Infinite flat plate model of the structure of a tire with smear tread pattern representation.*

In this case, w is the normal surface displacement of the plate and $f(t)\delta(x - x_f)$ $\delta(y - y_f)$ defines a time-dependent input point force located at (x_f, y_f). Orthotropic structural properties are also assumed. Thus, different bending stiffnesses along the transversal, circumferential, and cross directions are assigned. These are defined as $B_y(y)$, B_x, and B_{xy}, respectively. Note that these account for nonuniformities along the transversal direction of the tire, given that both the bending stiffness $B_y(y)$ and the plate's mass per unit area $m(y)$ depend on y (the transversal direction coordinates of the tire). The latter includes the added mass of the tread band with a smear representation of the tread pattern. This approach is similar to that implemented in the work by Pinnington [*10*,*11*].

In an effort to include the effects of rotation, the plate is assumed to be moving along the circumferential direction (positive x axis) with a velocity V_p. This translational velocity can be calculated as $V_p = \Omega \times a$, where Ω is the tire's rotational velocity in [rad/s] and a is the tire's outer circumference radius. The last two terms on the left-hand side of Eq. (1) account for this velocity, as proposed by Lee [*12*]. Finally, inflation pressure can be accounted for with membrane tensions along both the transversal and circumferential directions. These can be calculated as $T_{0x} = pa$ and $T_{0y} = pa/2$, respectively, and are included in the first two terms on the left-hand side of Eq. (1).

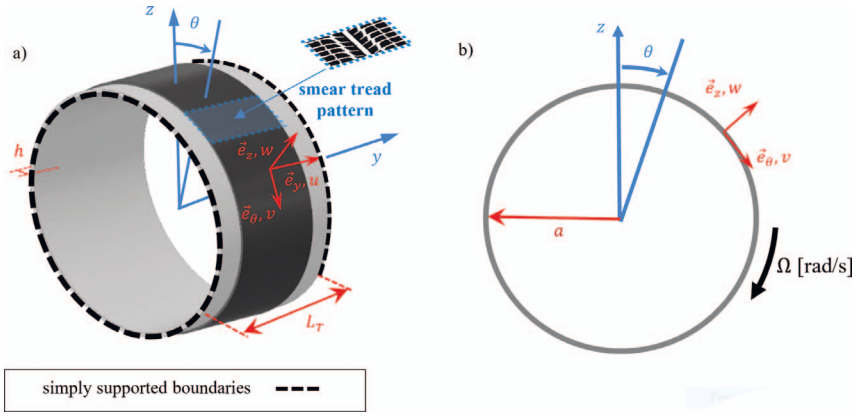

FIG. 3 — *Cylindrical shell model of the structure of a tire.*

Cylindrical Shell Model

In an effort to include the effects of curvature in the structural model, the tire is modeled with the cylindrical shell shown in Fig. 3. It is assumed that it is simply supported at its two transversal boundaries. This simulates real working conditions, in which the tire is mounted on a wheel. The dynamic response of the shell is defined in terms of three mid-surface displacement components, in accordance with Kirchhoff's hypothesis [*13*]. Thus, u corresponds to the transversal displacements along the y axis, v corresponds to the displacements tangential to the shell's curvature defined by the angle θ, and w corresponds to the radial displacements along the z axis. In addition, the shell's radius is defined by a, its thickness by h, and its transversal length L_T.

The shell is assumed to follow the Donnell-Mushtari-Vlaslov theory. In such a case, the mid-surface displacements on the shell's tangent plane and their derivatives have negligible effects in its curvature and twist. In addition, further simplifications are proposed for vibration-induced noise applications. These assume that the motion of the tire is dominated by radial vibrations, thus rendering the inertia effects on its tangent plane negligible. Finally, it is also assumed that the shell's radius is much larger than its thickness.

A shell that follows the simplifications defined above is typically referred to as a shallow shell. In the work by Soedel [*14*], it was demonstrated that these simplifications provide very good modal approximations if compared with classic Love theory for isotropic shells defined in [*13*]. Still, slight inaccuracies are expected only at low frequencies, well below the range of interest in this study.

The resulting equation of motion of the cylindrical shell is defined solely in terms of the normal surface displacement of the shell $w(\theta, y)$ and is defined as follows

$$\begin{aligned}
&\alpha_1 \frac{\partial^6}{\partial y^2 \partial \theta^4}\left(D_{11}(y)\frac{\partial^2 w}{\partial y^2}\right) + \alpha_2 \frac{\partial^6}{\partial y^6}\left(D_{11}(y)\frac{\partial^2 w}{\partial y^2}\right) \\
&+ \alpha_3 \frac{\partial^6}{\partial y^4 \partial \theta^2}\left(D_{11}(y)\frac{\partial^2 w}{\partial y^2}\right) + \left(\chi_2 - D_{11}(y)\alpha_3\right)\frac{\partial^8 w}{\partial y^6 \partial \theta^2} \\
&+ \left(\chi_3 - D_{11}(y)\alpha_1\right)\frac{\partial^8 w}{\partial y^4 \partial \theta^4} + \chi_4 \frac{\partial^8 w}{\partial y^2 \partial \theta^6} + \chi_5 \frac{\partial^8 w}{\partial \theta^8} + \frac{1}{a^2}\frac{\partial^4 w}{\partial y^4} \\
&- \omega^2\left(\alpha_1 m(y)\frac{\partial^4 w}{\partial \theta^4} + \alpha_2 \frac{\partial^4 m(y) w}{\partial y^4} + \alpha_3 \frac{\partial^4 m(y) w}{\partial y^2 \partial \theta^2}\right) \\
&- \frac{1}{a^2}\left(\alpha_1 N_\theta^r(y)\frac{\partial^6 w}{\partial \theta^6} + \alpha_2 \frac{\partial^6 N_\theta^r(y) w}{\partial y^4 \partial \theta^2} + \alpha_3 \frac{\partial^6 N_\theta^r(y) w}{\partial y^2 \partial \theta^4}\right) \\
&- N_y^r\left(\alpha_1 \frac{\partial^6 w}{\partial y^2 \partial \theta^4} + \alpha_2 \frac{\partial^6 w}{\partial y^6} + \alpha_3 \frac{\partial^6 w}{\partial y^4 \partial \theta^2}\right) \\
&+ 2i\omega\Omega\left(\alpha_1 m(y)\frac{\partial^3 w}{\partial \theta^3} + \alpha_3 \frac{\partial^3 m(y) w}{\partial y^2 \partial \theta} + \alpha_4 \frac{\partial^3 m(y) w}{\partial y^2 \partial \theta}\right) \\
&- \Omega^2\left(\alpha_1 m(y)\frac{\partial^4 w}{\partial \theta^4} + \alpha_2 \frac{\partial^4 m(y) w}{\partial y^4} + \alpha_3 \frac{\partial^4 m(y) w}{\partial y^2 \partial \theta^2}\right) \\
&= \left(\alpha_1 \frac{\partial^4 F_r}{\partial \theta^4} + \alpha_2 \frac{\partial^4 F_r}{\partial y^4} + \alpha_3 \frac{\partial^4 F_r}{\partial y^2 \partial \theta^2}\right) \qquad (2)
\end{aligned}$$

The multiplying constants in Eq. (2) are defined as

$$\alpha_1 = \frac{K_{22}}{a^4(K_{11}K_{22} - K_{12}^2)} \qquad \alpha_2 = \frac{K_{11}}{K_{11}K_{22} - K_{12}^2}$$
$$\alpha_3 = \frac{1}{a^2}\left(\frac{1}{K_{33}} - \frac{2K_{12}}{K_{11}K_{22} - K_{12}^2}\right) \qquad \alpha_4 = \frac{K_{12}}{a^2(K_{11}K_{22} - K_{12}^2)} \qquad (3)$$

and

$$\chi_2 = \left[\alpha_3 D_{11} + \frac{2\alpha_2(D_{12} + 2D_{33})}{a^2}\right]$$
$$\chi_3 = \left[\alpha_1 D_{11} + \frac{\alpha_2 D_{22}}{a^4} + \frac{2\alpha_3(D_{12} + 2D_{33})}{a^2}\right]$$
$$\chi_4 = \left[\frac{2\alpha_1(D_{12} + 2D_{33})}{a^2} + \frac{\alpha_3 D_{22}}{a^4}\right] \quad \chi_5 = \left(\frac{\alpha_1 D_{22}}{a^4}\right) \qquad (4)$$

In this case, all the stiffness terms defined with K and D are calculated as

$$[K] = \begin{bmatrix} E_y h & E_{y\theta} h & 0 \\ E_{y\theta} h & E_\theta h & 0 \\ 0 & 0 & Gt \end{bmatrix} \qquad [D] = \begin{bmatrix} \frac{E_y h^3}{12} & \frac{E_{y\theta} h^3}{12} & 0 \\ \frac{E_{y\theta} h^3}{12} & \frac{E_\theta h^3}{12} & 0 \\ 0 & 0 & \frac{Gh^3}{12} \end{bmatrix} \tag{5}$$

where E_y is the elastic modulus along the transversal direction, E_θ along the circumferential direction, and $E_{y\theta}$ along the cross direction. In addition, G is the shear modulus of the tire's composite material. Further details on how Eq. (2) was derived can be found in [*15*].

The nonuniformities along the transversal direction are accounted for in Eq. (2) with $D_{11}(y)$ and $m(y)$. The rotational velocity is accounted for in terms that include Ω [rad/s]. Finally, inflation pressure is accounted for as it was done for the infinite plate. That is, with membrane tensions. In this case, these are included in the term $N_\theta^r(y) = pa + m(y)a\Omega^2$ along the circumferential direction and $N_y^r = pa/2$ along the transversal direction of the tire.

Full-Wave Propagation Response

In this section, the formulation to find the structural response of a tire using a full-wave propagation response is presented. The response consists of modes in the transverse direction and waves in the circumferential direction, defined in a generic form as follows:

$$w(\xi, y, t) = \sum_n^N q_n \phi_n(y) X_n(\xi) e^{i\omega t}$$

$$\begin{aligned} &...\xi \text{ corresponds to } x \text{ for the flat plate model} \\ &\quad \xi \text{ corresponds to } \theta \text{ for the cylindrical shell model} \end{aligned} \tag{6}$$

where the generic coordinate ξ corresponds to x for the plate models and θ for the cylindrical shell model. Along this direction, a full-wave propagation is assumed of the form $X_n(\xi) = e^{-ik_\xi \xi}$. On the other hand, y is the coordinate along the transversal direction. Along this direction, a total of N transversal modes are defined with a modal amplitude q_n and a function $\phi_n(y)$. The latter is computed in terms of admissible functions that satisfy the essential boundary conditions. In this case, sine functions have been selected as follows:

$$\phi_n(y) = \sum_m^M A_{mn}\psi_m(y) = \sum_m^M A_{mn}\sin\left(\frac{m\pi y}{L_T} + \frac{m\pi}{2}\right) \tag{7}$$

where A_{mn} are the corresponding admissible function amplitudes associated with the m^{th} function and n^{th} transversal mode. These admissible amplitudes are found by defining an eigenvalue problem using the homogeneous equation of motion of the tire. For the flat plate model, this is

$$\frac{\partial^2}{\partial y^2}\left(B_y(y)\frac{\partial^2 w}{\partial y^2}\right) - m(y)\frac{\partial^2 w}{\partial t^2} = 0 \tag{8}$$

On the other hand, for the cylindrical shell model, it is defined as

$$\alpha_2\frac{\partial^6}{\partial y^6}\left(D_{11}(y)\frac{\partial^2 w}{\partial y^2}\right) + \chi_6\frac{\partial^4 w}{\partial y^4} - N_y^r\alpha_2\frac{\partial^6 w}{\partial y^6} - \Omega^2\alpha_2\frac{\partial^4 m(y)w}{\partial y^4} - \omega^2\alpha_2\frac{\partial^4 m(y)w}{\partial y^4} = 0 \tag{9}$$

Eq. (7) is substituted in the appropriate homogeneous equation. The resulting expression is then premultiplied by a vector of admissible functions and integrated over the transversal direction y. The outcome is an eigenvalue problem, and its solution defines the transversal modes of the tire. This is an approximation; however, an exact solution is possible if all the terms on the equations of motion are used to construct the homogeneous equations and the eigenvalues solved for all wave numbers k_ξ. This would be a very computationally intensive approach.

Once the transversal modes are known, the full-wave propagation solution to the equations of motion (1) and (2) is then applied as follows:

1. Substitute Eq. (6) (the assumed solution) into the desired structural equation of motion.
2. Premultiply by $\phi_n(y)$, integrate over y, and perform wavenumber transform. After this process, the following generic system is obtained

$$\left[\sum_m^M [C_m]k_\xi^m + [\lambda_n] - \omega^2[I]\right]\left\{q_n X_n(k_\xi)\right\} = \left\{F_n(k_\xi)\right\} \tag{10}$$

where k_ξ^m corresponds to the wavenumber along the circumferential direction elevated to the m^{th} power. In this case, m is associated with the m^{th} derivative with respect to ξ in the equation of motion. Each of the m^{th} expressions is associated to a stiffness matrix defined as $[C_m]$. On the other hand, $[\lambda_n]$ is a diagonal matrix containing the eigenvalues (squared transversal natural frequencies of the tire), $[I]$ is the identity matrix, and finally $\{F_n(k_\xi)\}$ is a vector containing all modal forces.

3. Decouple the system in Eq. (10) by only accounting the diagonal terms of matrices $[C_m]$, and then perform an inverse wavenumber transform as follows:

$$q_n X_n(\xi) = \frac{1}{2\pi}\int_{-\infty}^{\infty} \frac{F_n(k_\xi)e^{-ik_\xi \xi}}{\sum C_{m,n}k_\xi^m + \lambda_n - \omega^2}\, dk_\xi \tag{11}$$

where $C_{m,n}$ correspond to the n^{th} diagonal value of the matrix $[C_m]$ associated with the n^{th} transversal mode. Finally, now that $q_n X_n(\xi)$ is known, it can be substituted back into the assumed solution in Eq. (6) to find the response of the tire.

?2 The mobility FRF of the tire can also be computed. This is performed by multiplying the normal surface displacement defined in Eq. (6) by $i\omega$ and dividing by the input harmonic force with amplitude F_0.

The resulting mobility FRF for the infinite flat plate model computed at a location (x_t, y_t) due to excitation at a point (x_f, y_f) then becomes

$$M_{IP}\Big((x_t, y_t)|(x_f, y_f), \omega\Big) = \frac{i\omega}{F_0}\sum_n^N \phi_n(y_t)\frac{1}{2\pi}\int_{-\infty}^{\infty} \frac{F_n(k_x)e^{-ik_x x_t}}{C_{IP,n}(k_x, \omega)}\, dk_x \tag{12}$$

for $n = 1, 2, 3, \ldots N$ transversal modes and circumferential wave numbers k_x from $-\infty$ to $+\infty$.

In this case, $C_{IP,n}(k_x, \omega) = \Big(C_{xx,n}k_x^4 + C_{xy,n}k_x^2 + C_{V,n}\omega k_x + \omega_n^2(1 + i\eta_n) - \omega^2\Big)$, where $C_{xx,n}$, $C_{xy,n}$, and $C_{V,n}$ correspond to correspond to the n^{th} diagonal values of the associated stiffness matrices. On the other hand, the mobility FRF and for the cylindrical shell computed at a location (θ_t, y_t) due to excitation at a point (θ_f, y_f) becomes

$$M_{CS}\Big((\theta_t, y_t)|(\theta_f, y_f), \omega\Big) = \frac{i\omega}{F_0}\sum_n^N \phi_n(y_t)\frac{1}{2\pi}\int_{-\infty}^{\infty} \frac{F_n(k_\theta)e^{-ik_\theta \theta_t}}{C_{cs,n}(k_\theta, \omega)}\, dk_\theta \tag{13}$$

for $n = 1, 2, 3 \ldots N$ transversal modes and circumferential wave numbers k_θ from $-\infty$ to $+\infty$.

In this case,

$$\begin{aligned} C_{cs,n}(k_\theta, \omega) = {} & C_{1,n}k_\theta^8 + C_{2,n}k_\theta^6 + C_{3,n}k_\theta^4 + C_{4,n}k_\theta^2 + \omega_n^2(1 + i\eta_n) + \omega C_{5,n}k_\theta^3 \\ & + \omega C_{6,n}k_\theta - \omega^2 N_{1,n}k_\theta^4 - \omega^2 N_{2,n}k_\theta^2 - \omega^2 \end{aligned}$$

where $N_{1,n}$, $N_{2,n}$, and $C_{1,n}$ through $C_{6,n}$ correspond to the n^{th} diagonal values of

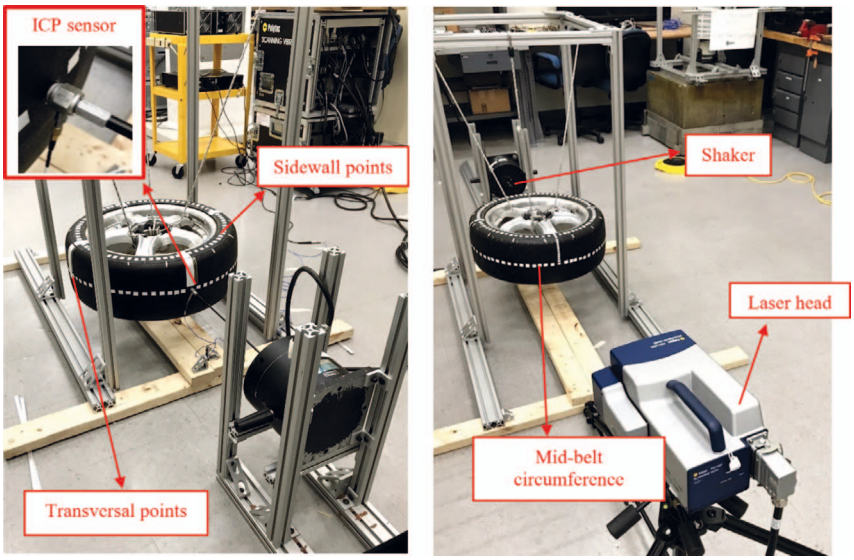

FIG. 4 — *(a) Tire hanged in experimental rig and shaker. (b) Laser vibrometer head pointing toward the tire belt.*

the associated stiffness matrices. Further details about this formulation can be found in [*15*].

In addition, it can be observed that for both mobility functions, additional modal damping has been added with the modal loss factor $_n$. Finally, the forcing term in Eq. (12) is the following

$$F_n(k_x) = F_0 e^{ik_x x_f} \phi_n(y_f) \tag{14}$$

while the forcing term in Eq. (13) is

$$F_n(k_\theta) = F_0 e^{ik_\theta \theta_f} \left[\alpha_1 \phi_n(y_f) k_\theta^4 + \alpha_2 \frac{\partial^4 \phi_n(y_f)}{\partial y^4} - \alpha_3 \frac{\partial^2 \phi_n(y_f)}{\partial y^2} k_\theta^2 \right] \tag{15}$$

Structural Response Validation

To validate modeled structural responses of a tire for the frequency range of interest, an experiment was performed. A slick tire of size 225/45R17 was used. The tire was inflated to 32 psi and hanged horizontally with elastic chords, as shown in Fig. 4. A Bruel & Kjaer permanent magnetic vibration exciter type 4808 was used to excite the tire. A stinger was connected between the shaker and a point located at the center of the tire's belt. In addition, an ICP force sensor PCB208C02 was fitted to the tip of the stinger and glued to the tire's

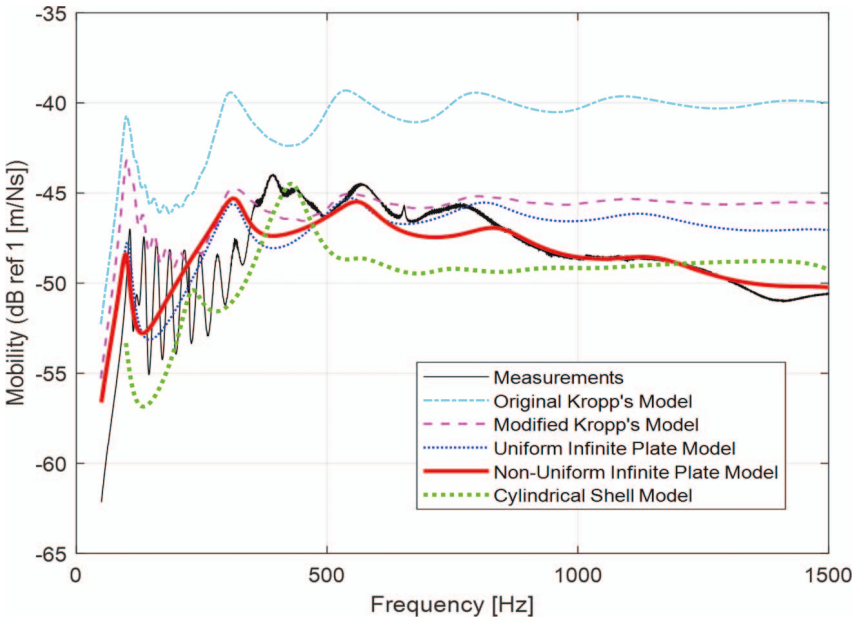

FIG. 5 — *Measured and simulated mobility FRFs measured at a point located at 1 cm above the excitation location for a tire of size 225/45R17 (approximated input mobility FRF).*

surface, as shown in Fig. 4a. This allowed for measuring the actual input force that excites the tire at the input location.

A total of 199 points were marked on the tire surface with retroreflective tape. The response of the tire at these points was measured with a Polytec PSV-400 scanning laser vibrometer, as shown in Fig. 4b. Seventy-one of the marked points were located along the mid-belt circumferential line of the tire. Therefore, its dynamic response was measured at every 5° along the belt's circumference. It should be noted that it was not possible to measure the response at the point of excitation. Another 72 points were marked at the top sidewall of the tire. Finally, the response of the tire was also measured at 14 points along its transversal direction, including the belt and sidewalls. This was done at 0°, 90°, 180°, and 270° from the excitation location.

Only the measured input mobility FRFs are analyzed here. However, because the response could not be measured at the exact point of excitation, approximated results for a point at 1 cm above the excitation location will be used for the comparisons. Figure 5 shows the simulated input mobility of FRFs using the structural modeling approaches presented in the previous sections. These are compared with the measured mobility FRF at the same location.

TABLE 1 — *Uniform and nonuniform tire parameters used for FRF simulations.*

Parameter	Notation	Tire part, direction	Value [units]
Nonuniform case			
Mass per unit area	m_b	Belt	17.4 [kg/m^2]
Mass per unit area	m_s	Sidewalls	12.3 [kg/m^2]
Bending stiffness	B_{yb}	Belt, y-direction	6.9 [Nm]
Bending stiffness	B_{ys}	Sidewalls, y-direction	1.2 [Nm]
Uniform case			
Mass per unit area	m	Belt and sidewalls	16 [kg/m^2]
Bending stiffness	$B_{x,\theta}$	Belt and sidewalls, x or θ	6 [Nm]
Bending stiffness	B_y	Belt and sidewalls, y-direction	4.05 [Nm]
Membrane tension	$T_{0x,\theta}$	Belt and sidewalls x or θ (32 psi)	3.49×10^4 [N/m]
Membrane tension	T_{0y}	Belt and sidewalls, y-direction (32 psi)	6.99×10^4 [N/m]

The results presented in Fig. 5 are shown for a frequency range of up to 1500 Hz for completeness. However, simulated results are only comparable with measurements within 500 Hz to 1500 Hz. The reason for this is that the structural models were constructed to be accurate exclusively for this range. Finally, all of the structural properties of the tire for this validation case are shown in Table 1 for a transversally uniform and nonuniform tire structure. These were defined as follows. First, an initial baseline for the parameters was used according to those reported by Pinnington and Briscoe [*16*] and Kim et al. [*17*]. These were then modified until a reasonable fit was attained between the measurements and the modeled mobility functions. For example, based on experiments, Pinnington and Briscoe [*16*] reported an average mass per unit area of a typical passenger car tire to be 16 kg/m^2. This was used as m in Table 1. The masses for the belt and sidewalls were then defined so that $(m_b + m_s)/2 \approx m$. A similar process was followed to define the stiffnesses, using as baseline the parameters defined by Kim et al. [*17*]. Finally, as specified in [15], the membrane tensions were approximated using the tire's inflation pressure and outer radius, as $T_{0y} = pa/2$ and $T_{0x,\theta} = pa$, respectively.

For comparison purposes, Fig. 5 shows the response of the tire predicted with a full-modal approach presented in the work by Kropp [*7*] and a modified version proposed by Perisse et al. [*18*]. For the first case, a cross-stiffness $B_{xy} = \sqrt{B_x B_y} = 4.93$ Nm was used, and for the second case, a much higher cross-stiffness of $B_{xy} = 130$ Nm was implemented, as proposed by [*18*]. When compared with measurements, it can be observed that both approaches overpredict the response, especially for frequencies greater than 750 Hz. Further details about these modal approaches can be found in [*19*].

Figure 5 also shows the response computed using the full-wave propagation approach of the infinite flat plate model. If uniform properties along the tire's

transverse direction are used, improved accuracy over the high-frequency range is observed when compared with the modal approaches. Still, the most accurate results are obtained when nonuniformities are introduced. Very good agreement with the experimental data is shown between 800 Hz and 1300 Hz (i.e., most of the frequency range of interest). This shows that including nonuniformities across the tire's transversal direction is important to model the tire's response with improved accuracy.

On the other hand, Fig. 5 also shows that the response predicted with the nonuniform infinite plate is better than that obtained with the cylindrical shell model, especially between 500 Hz and 800 Hz. Still, the cylindrical shell model is more accurate between 300 Hz and 500 Hz, even though this is out of the frequency range of interest. This is probably because this model includes curvature effects, which are important below the tire's ring frequency (usually located around 500 Hz).[7] However, it should be noted that the accuracy of the cylindrical shell depends on how well the input structural parameters are selected. This is a challenging task, and future work should be directed to address this. A proposed alternative is to combine the cylindrical shell model for frequencies between 300 and 500 Hz and the nonuniform flat plate model for frequencies greater than 500 Hz. This should result in predictions with improved accuracy for a wider frequency range.

Tread Pattern Excitation Forces

To properly model tread pattern excitation forces between the tire and the pavement during rolling conditions, a new frequency domain formulation is proposed in this section. These are then coupled to the desired structural tire model presented above. The first step is to calculate the contact forces in the time domain for a single block, as it passes through the contact patch. To do this, the model for rectangular nonskewed blocks proposed by Liu [*20*,*21*] was implemented. Thus, tread pattern blocks need to be approximated with a rectangular shape, as shown in the unwrapped tread pattern view in Fig. 6b.

The tread pattern block enters the contact patch leading edge (LE) and exits later at the trailing edge (TE). Figure 6b shows the approximated contact patch region. Each block develops a force normal to the tire surface as it enters the LE, then increases and stabilizes for a brief period of time. Finally, it decreases to zero when leaving the contact patch at the TE. During the block-pavement contact, other forces will also be present (i.e., tangential forces due to longitudinal friction). An example of such forces for a single rectangular block is shown in Fig. 7.

The modeling approach initially developed by Liu [*20*,*21*] and implemented here discretizes each block into a set of normal and tangential spring elements. The forces are computed as follows:

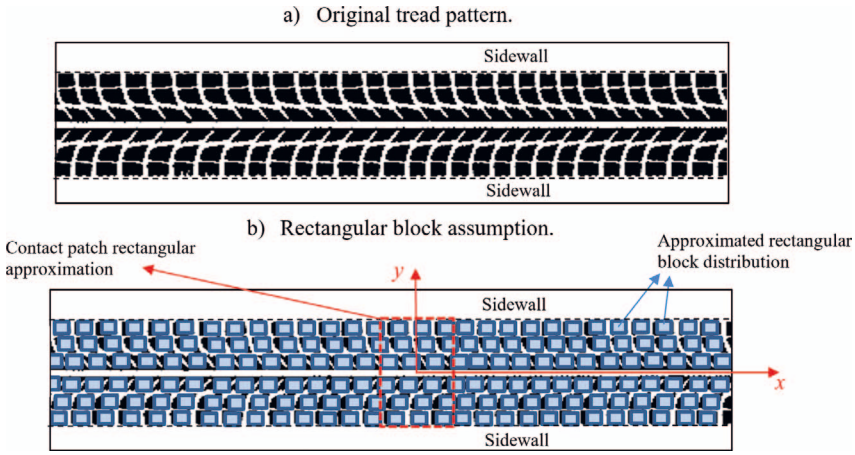

FIG. 6 — *Approximated block distribution in tread pattern using a rectangular block assumption.*

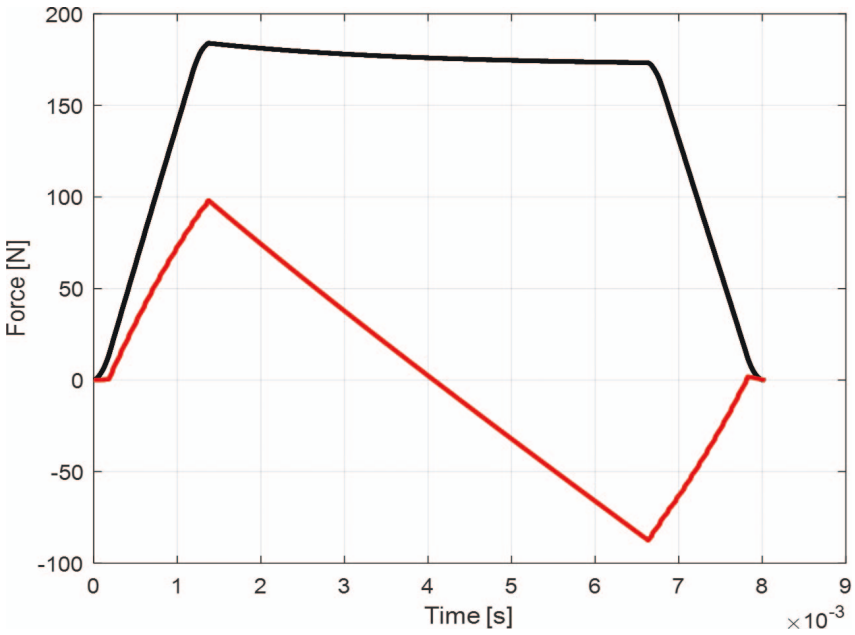

FIG. 7 — *Normal (black) and tangential (red) forces applied on a single block as it passes through the contact patch.*

$$f_B\left(x_b(t), y_b, t\right) = \int_{-\infty}^{t} \frac{E(t-\tau) d_{bx} d_{by}}{n h_t} \frac{d\delta}{d\tau} d\tau$$

$$f_T\left(x_b(t), y_b, t\right) = \int_{-\infty}^{t} \frac{E(t-\tau) d_{bx} d_{by}}{2(1+\nu) h_t n} \frac{d\chi}{d\tau} d\tau \tag{16}$$

where $E(t) = E_0 + \left(1 - \sum_{i=1}^{N} p_i \left(1 - e^{-(t/\tau_i)}\right)\right)$, $N = 1, 2, 3....$ is the block's time-dependent elastic modulus defined in terms of a Prony series coefficients p_i and τ_i, whereas δ and χ are the spring normal and tangential time-dependent deflections, respectively, as it enters and exits the contact patch.

To account for the slip of the block, the following friction law is solved to find the tangential block deflections:

$$\frac{d\chi}{dt} = \xi V_0 \qquad |f_T\left(x_b(t), y_b, t\right)| \leq \mu_s f_B\left(x_b(t), y_b, t\right)_r \text{(no slip condition)}$$

$$\bar{m}\frac{d^2\chi}{dt^2} + f_T\left(x_b(t), y_b, t\right) = \text{sign}\left(\xi V_0 - \frac{d\chi}{dt}\right)$$

$$\mu_k f_B\left(x_b(t), y_b, t\right) |f_T\left(x_b(t), y_b, t\right)| > \mu_s f_B\left(x_b(t), y_b, t\right) \text{(slip condition)} \tag{17}$$

In this case, $\bar{m} = M/n$, where M is the total mass of the block. On the other hand, the kinetic friction coefficient between the road and the rubber block is defined as $\mu_k(p, \xi V_0) = \frac{\alpha |p|^{\eta-1} + \beta}{a + b|\xi V_0|^{-\frac{1}{k}} + c|\xi V_0|^{-\frac{2}{k}}}$. Further details about this model can be found in [*20*,*21*]. All of the modeling parameters for the simulated forces shown in Fig. 7 are summarized in Table 2. In this case, the Prony series constants, kinetic friction law parameters, and others were obtained from the literature [*22*,*23*]. Further details about this model can be found in [*20*,21].

Even though tangential and normal forces are excited for every single block as it enters and exits the contact patch, only the normal component is coupled with the structural model. The reason is that during steady-state rolling conditions, tangential forces will produce small out-of-plane motion. Thus, the tangential forces are small if compared with the normal ones, as shown in the work by Liu et al. [*21*]. Furthermore, it is thought that, since the structural vibrations of the tire are dominated by its bending components, the effects of tangential input forces may be neglected.

The normal force is moving relative to a stationary structural coordinate system and is changing its amplitude as it travels through the contact patch (see Fig. 6b). An observer moving with the block will see a time-dependent moving

TABLE 2 — *Input parameters for the block contact model.*[a]

Parameter	Sign	Value [units]
Maximum block compression	Δ	0.2[mm]
Belt velocity	V_r	60[mph]
Creep ratio	ξ	0.3%
Block density	ρ_b	1000 [kg/m^3]
Block material Poisson's ratio	V	0.47
Block surface area	$A_b = d_{bx} \times d_{by}$	5 [cm^2]
Block height	h_t	0.8 [cm]
Kinetic friction law parameters (rubber on concrete surface)	α	0.1399
	β	0.4091
	η	0.8680
	$\left(\frac{1}{\kappa}\right)$	0.1672
	a	0.9203
	b	−1.1188
	c	0.9677
Elastic modulus Prony series coefficients	E_0	3.3×10^6 [Pa]
	p_1	0.487
	p_2	0.137
	τ_1	9.96×10^{-5} [s]
	τ_2	1.20×10^{-3}[s]
Tire radius at contact patch edges	R_d	0.5 [m]
Contact patch length	ℓ	0.17 [m]
Block contact pressure	P	0.4 [N/mm^2]
Number of springs per block	n	100

[a]Prony series coefficients obtained from the work by Lopez Arteaga [*22*]. Friction law parameters obtained from the work by Hofstetter et al. [*23*].

force. This force is defined as $f_B(x_b(t),\ y_{b,}\ t)$, in terms of the block time-dependent circumferential location $x_b(t)$, transversal location y_b, and time t. This force is then approximated in discrete time and space as an impulse train with time-changing amplitudes, as shown in Fig. 8.

The modeled normal force is discretized in a set of time intervals Δt between the time at which the block enters the contact patch t_i and the time at which it exits t_e. The force is evaluated at the discrete times t_k, defined at the center of each interval as $t_k = \frac{(x_{LE}-x_b)}{V_T} + (k - 1/2)\Delta t$ for $k = 1, 2, \cdots, N_k$. In this case, x_{LE} is the location along the x axis of the LE of the contact patch, and V_T is the velocity of the traveling block. Thus, the impulse train is defined by

$$f_b\Big(x_b(t), y_b, t\Big) \approx \sum_{k=1}^{N_k} f_B(x_k, y_b, t_k)\Delta t\delta(t - t_k)\delta(x - x_k)\delta(y - y_b) \tag{18}$$

where $x_k = x_{LE} + V_T(t_k - t_i) = x_{LE} + V_T(k - 1/2)\Delta t$. The impulses $f_B(x_k,\ y_b,\ t_k)$ $\Delta t\delta(t - t_k)$ are defined at fixed locations $(x_k,\ y_b)$ within the contact patch. These locations are referred to as the contact patch excitation points defined as the block enters, passes through, and finally leaves the contact patch.

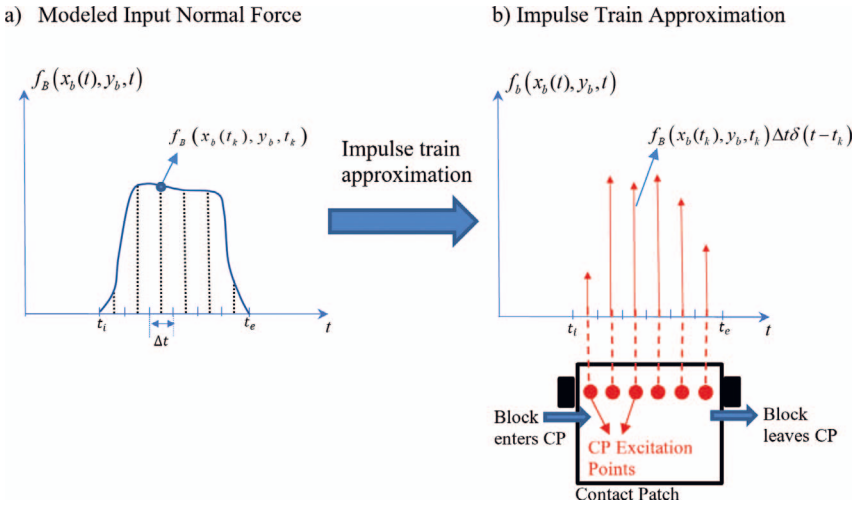

FIG. 8 — *(a) The modeled behavior of time moving force applied to a single block. (b) Approximation of force behavior using an impulse train and associated contact patch excitation points.*

Using the discrete Fourier transform (DFT) pair for the special case of an impulsive time function, the block force in the time domain then becomes

$$f_b\Big(x_b(t), y_b, t\Big) \approx \sum_{k=1}^{N_k} \left\{ \sum_{n=-N}^{n=N} \frac{\omega_T}{2\pi} f_B(x_k, y_b, t_k) \Delta t e^{-in\omega_T t_k} e^{in\omega_T t} \right\} \delta(x - x_k)\delta(y - y_b) \tag{19}$$

where the rotational frequency of the tire is defined as $\omega_T = \frac{2\pi V_T}{l_T}$ (ℓ_T is the outer circumference of the tire). The complex amplitude (DFT coefficient) for each impulse is

$$F_b^{kn}\Big(x_b(t), y_b, n\omega_T\Big) = \frac{\omega_T}{2\pi} f_B(x_k, y_b, t_k) \Delta t e^{-in\omega_T t_k} n = \pm 1, \pm 2, , \cdots, \pm N \tag{20}$$

The next step is to extend the formulation shown above from a single block to the full tread pattern (i.e., multiple blocks). The most important consideration in modeling a tread pattern is to properly account for the relative time delay of the block forces. Certain guidelines are defined for a tread pattern. It consists of N_r circumferential arrays of blocks (ribs) at different y transversal positions, for example, y_r for $r = 1, 2, \ldots, N_r$ ribs. Each array has N_{br} number of blocks, which can be evenly or irregularly distributed. The x-position of the blocks in the array will be defined by setting the coordinate of one block x_1^r and then defining the relative position of the other blocks. Thus, the coordinate of the m^{th} block in the r^{th} rib becomes $x_m^r = x_1^r + \Delta x_m^r$. To account for the time delay between arrays,

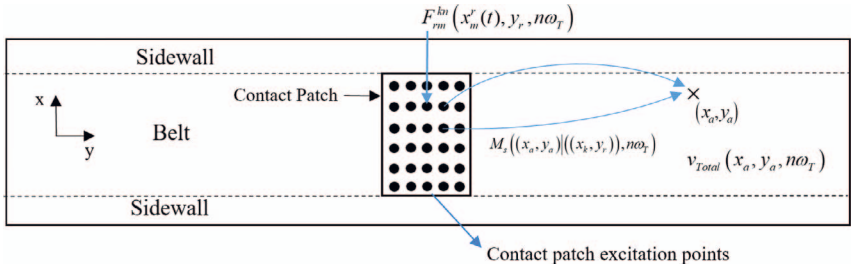

FIG. 9 — *Method used to couple the input excitation forces and the response of the tire (i.e., normal surface velocities at any arbitrary location on the tire surface).*

the coordinate of the first block in each array is defined relative to the first block of the first array.

Using the guidelines above, the DFT pair for the time domain forces acting on the k^{th} contact patch excitation point of the r^{th} rib due to the m^{th} block is approximated as

$$f_m^r\left(x_m^r(t), y_r, t\right) \approx \sum_{k=1}^{N_k}\left\{\sum_{n=-N}^{n=N}\frac{\omega_T}{2\pi}f^r\left(x_k, y_r, (t_m^r)_k\right)\Delta t e^{-in\omega_T(t_m^r)_k}e^{in\omega_T t}\right\} \times \delta(x - x_k)\delta(y - y_r) \tag{21}$$

where $f^r(x_k, y_r, (t_m^r)_k)$ is the modeled block force at discrete k times $(t_m^r)_k$ for the r^{th} rib. In this case, the complex amplitudes (DFT coefficients) are defined as follows:

$$F_{rm}^{kn}\left(x_m^r(t), y_r, n\omega_T\right) = \frac{\omega_T}{2\pi}f^r\left(x_k, y_r, (t_m^r)_k\right)\Delta t e^{-in\omega_T(t_m^r)_k} n = \pm 1, \pm 2, , \cdots, \pm N \tag{22}$$

Finally, the tread pattern forcing function in the frequency domain in Eq. (22) is coupled with the structural response of the tire. The complex amplitude response at any arbitrary location (x_a, y_a) on the tire surface is computed using the product of the mobility function of the tire structure (either Eq. (12) or (13) for the plate and shell models) and the forcing function in Eq. (22). This coupling process is shown in Fig. 9 and mathematically defined as follows:

$$v_{Total}(x_a, y_a, n\omega_T) \approx \sum_{r=1}^{N_r}\sum_{m=1}^{N_{br}}\sum_{k=1}^{N_k}\frac{\omega_T}{2\pi}f^r\left(x_k, y_r, (t_m^r)_k\right)\Delta t e^{-in\omega_T(t_m^r)_k} \times M_s\left((x_a, y_a)|\left((x_k, y_r)\right), n\omega_T\right) \tag{23}$$

where $v_{Total}(x_a, y_a, n\omega_T)$ corresponds to the normal surface velocity of the tire surface at a location (x_a, y_a) and a frequency $n\omega_T$.

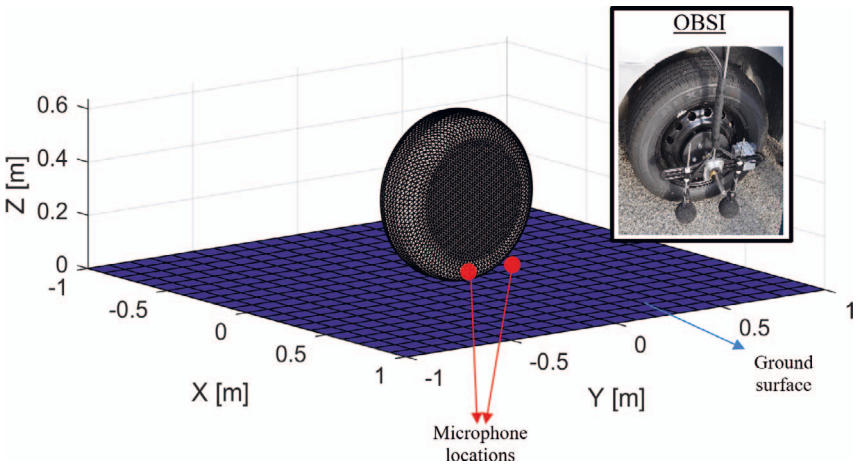

FIG. 10 — *Field points at the leading and trailing edge locations in front of the tire sidewall (same locations as OBSI).*

Finally, it should be noted that the total force time history over the contact patch is then the contribution of all the ribs. Thus, the total load applied in the contact patch is the following:

$$f_{cp}(t) = \sum_{k=1}^{N_k} \sum_{r=1}^{N_r} \sum_{m=1}^{N_{br}} f^r\left(x_k, y_r, (t_m^r)_k\right) \Delta t \delta\left(t - (t_m^r)_k\right) \tag{24}$$

This must be constant at all times during steady-state rolling conditions and equal to the load applied to the tire by the vehicle.

Tread Pattern Noise Demonstration

A BEM code, initially developed by Wu [*24*], was implemented to compute noise. Noise was predicted at two locations, as marked in Fig. 10 in red. These correspond to two trailing and LE locations relative, the same as those used for OBSI and specified in the standard AASHTO [*25*]. Thus, predicted noise can be compared with measurements made with OBSI.

Structural simulations were performed using the nonuniform infinite plate structural model (i.e., the most accurate approach within the mid-frequency range). The structural parameters used are those provided in Table 1. A tire size of 215/60R16 and an inflation pressure of 32 psi was used with a total contact patch load of 2940 N (obtained from the test vehicle weight). The contact forces were computed using the parameters summarized in Table 2 (except for the maximum block compression and velocity, which were defined according to the test vehicle load and the set test velocities).

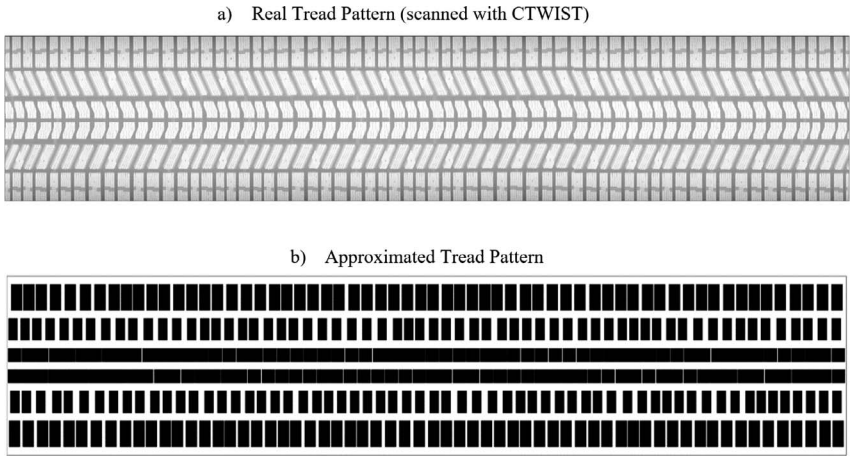

FIG. 11 — *(a) Real and (b) approximated tread patterns for a tire of size 215/60R16.*

A real tread pattern was approximated by using rectangular blocks of similar size to the real tread pattern and randomizing their distribution within each rib. Both the real and the approximated tread patterns are shown in Fig. 11.

Figure 12 shows the predicted and the measured A-weighted noise levels at the leading and TE locations for a velocity of 70 mph. In this case, only the tread pattern component of the measured noise was used for comparisons (further information about the separation of tread-pattern and non–tread-pattern noise components from OBSI measurements can be found in [*2*,*3*]). The results show that in both the leading and TE cases, the predicted noise levels are higher than those measured for most frequencies. This could be because of the approximations made for the tread pattern and rectangular contact patch. Still,

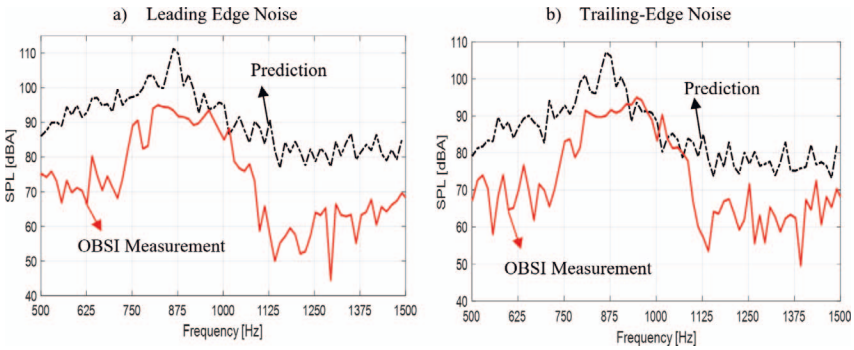

FIG. 12 — *Predicted and measured tread pattern noise for (a) leading edge and (b) trailing edge noise for a tire of size 215/60R16 (frequency resolution 13.92 Hz).*

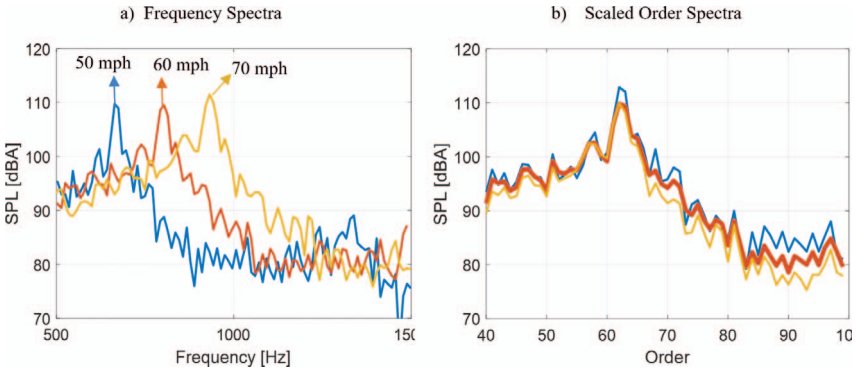

FIG. 13 — *(a) Tread pattern noise simulation spectra at three different speeds (50, 60, 70 mph). (b) Order spectra for the three speeds scaled to 60 mph.*

the results in Fig. 12a and Fig. 12b show that the measured and predicted noise levels agree very well between 900 and 1100 Hz. Finally, both measurements and predictions show similar spectral shapes. Their dominant frequency content is located between 800 and 1100 Hz. In addition, their initial slope toward the maximum noise levels is less significant than the negative slope toward high frequencies.

In an effort to analyze the behavior of tread pattern noise for different vehicle speeds, additional simulations were performed. The same inputs implemented to obtain the results in Fig. 12 were used. Tread pattern noise was predicted at the leading-edge microphone location for 50 mph, 60 mph, and 70 mph, as shown in Fig. 13a. It can be observed that noise amplitudes depend on the rotating speed of the tire. In general, higher speeds produce higher noise levels. The same behavior was observed on the measured tread pattern noise, as specified in [*2*]. In this case, measurements showed that the amplitude of tread pattern noise scales with speed with a scaling factor of 4. Therefore, if the noise levels at a reference velocity v_{ref} in mph are known, then the levels at any other speed v in mph can be calculated as follows:

$$L_p(v) = L_p(v_{\text{ref}}) + n \times 10\log_{10}\left(\frac{v}{v_{\text{ref}}}\right) \tag{25}$$

where n corresponds to the scaling factor. The performed simulation successfully captures the experimental scaling behavior. Figure 13b shows the frequency spectra at different speeds, transformed to order spectra. In addition, the simulated spectra for the three speeds have been scaled to 60 mph. It can be observed that all the amplitudes collapse, after applying Eq. (25) with the experimentally obtained scaling coefficient $n = 4$.

Conclusions

This study provides new modeling approaches for the prediction of vibration-induced tire noise. First, a wave propagation approach along the circumferential direction of the tire was implemented, in contrasts to assuming a full modal behavior. This formulation is new and has not been proposed in the available literature. Second, a tread pattern excitation model was presented. Its efficient frequency domain formulation is unlike classical approaches defined in the discrete time domain. Finally, results were compared with tire vibratory and noise measurements. This is the first time that the tread-pattern noise component from OBSI measurements has been compared with a full-wave propagation tire noise model.

The wave propagation method developed to determine the response of the tire within the frequency range of interest is the first of its kind. Circumferential traveling waves for all possible wave numbers between $-\infty$ and ∞ are accounted for in the model. Other modeling approaches simply select wave numbers for which an integer set of wavelengths can fit over the tire's circumference. This results in modes along the circumferential direction of the tire, thus ignoring the observed wave propagation behavior in typical responses of the tire. The tire responses modeled using this approach show that by accounting for structural nonuniformities along the transversal direction of the tire, a more accurate response can be obtained, especially within 800 to 1300 Hz. However, it was also shown that the additional effort to include a curvature with a cylindrical shell model did not render better results, except for a narrow frequency range between 300 and 500 Hz. Therefore, it can be concluded that the implementation of such a model it not justified because it is computationally demanding.

A new contact model that accounts for the proper tread pattern input to the tire's structure during rolling conditions was also presented. This is the first of its kind, as it is defined in the frequency domain. Common methods presented in the available literature are formulated in the time domain. These are less efficient when periodic inputs are used, such as a full tread pattern. The reason for this is that the response needs to be solved for multiple revolutions before the steady-state condition is reached. In addition, formulating the excitation of the tire in the frequency domain allows for the analysis of the excitation provided by different tread patterns. A tread pattern example was implemented. This was coupled with the structural model to determine the tire's response. Tread pattern noise was then predicted by implementing a boundary element algorithm. A comparison of predicted mid-frequency tread pattern noise and OBSI measurements was performed. The spectra showed very good agreement, especially between 900 and 1100 Hz at 70 mph. Furthermore, simulated noise scales with a velocity scaling factor of 4. This is the same behavior as seen in experimental tread pattern noise measurements.

Future research efforts should address the following. Measurements of the tire's structural response for rotating tires could allow for further exploration of the effects of rotation in the tire's response. In addition, transversal geometric effects in the tire's response should also be explored, for example, by implementing finite element models or using experimental data to find the transversal vibratory modes of the tire structure. Finally, additional methods to experimentally extract structural parameters should also be investigated.

Acknowledgments

This project was partially supported by the Center for Tire Research (CenTiRe), an NSF-I/UCRC (Industry/University Cooperative Research Centers) program led by Virginia Tech. The authors hereby wish to thank the project mentors and the members of the industrial advisory board of CenTiRe for their kind support and guidance.

References

[*1*] Li, T., "Literature Review of Tire-Pavement Interaction Noise and Reduction Approaches," *Journal of Vibroengineering*, Vol. 20, 2018, pp. 2424–2452.

[*2*] Li, T., "Tire-Pavement Interaction Noise (TPIN) Modeling Using Artificial Neural Network (ANN)," Ph.D. dissertation, Virginia Polytechnic Institute and State University, Blacksburg, VA, 2017.

[*3*] Spies, L., "A Machine-Learning Based Tool to Predict Tire Noise Using Both Tire and Pavement Parameters," master's thesis, Virginia Tech, Blacksburg, VA, 2019.

[*4*] Spies, L. D., McBride, S., Burdisso, R., and Sandu, C., "A Non-negative Artificial Neural Network Configuration for Noise Predictions," *Journal of the Acoustical Society of America*, Vol. 144, 2018, pp. 1756–1756.

[*5*] Donavan, P. R., and Oswald, L., *Quantification of Noise Mechanisms of Blank, Rib, and Cross-Bar Tread Bias-Ply Truck Tires*, General Motors Research Laboratories, Warren, MI, 1981.

[*6*] Bernhard, R., "Observations of the Structural Acoustics of Automobiles," Inter-Noise Congress and Conference, Nice, France, 2000.

[*7*] Kropp, W., "A Mathematical Model of Tyre Noise Generation," *International Journal of Heavy Vehicle Systems*, Vol. 1, 1999, p. 310.

[*8*] O'Boy, D. J., and Dowling, A. P., "Tyre/Road Interaction Noise—Numerical Noise Prediction of a Patterned Tyre on a Rough Road Surface," *Journal of Sound and Vibration*, Vol. 323, 2009, pp. 270–291.

[*9*] Hoever, C., "The Simulation of Car and Truck Tyre Vibrations, Rolling Resistance and Rolling Noise," Ph.D. dissertation, Chalmers University of Technology, Goteborg, Sweden, 2014.

[*10*] Pinnington, R. J., "A Wave Model of a Circular Tyre. Part 1: Belt Modelling," *Journal of Sound and Vibration*, Vol. 290, 2006, pp. 101–132.

[*11*] Pinnington, R. J., "A Wave Model of a Circular Tyre. Part 2: Side-Wall and Force Transmission Modelling," *Journal of Sound and Vibration*, Vol. 290, 2006, pp. 133–168.

[*12*] Lee, U., *Spectral Element Method in Structural Dynamics*, John Wiley & Sons, Singapore, 2009.

[*13*] Leissa, A. W., *Vibration of Shells*, Scientific and Technical Information Office, National Aeronautics and Space Administration, Washington, DC, 1973.

[*14*] Soedel, W., "Simplified Equations and Solutions for the Vibration of Orthotropic Cylindrical Shells," *Journal of Sound and Vibration*, Vol. 87, 1983, pp. 555–566.

[*15*] McBride, S., Burdisso, R., and Sandu, C., "A Non-uniform Cylindrical Shell Model for Tire-Pavement Interaction Noise Simulations," *INTER-NOISE and NOISE-CON Congress and Conference Proceedings*, Vol. 259, 2019, pp. 5927–5938.

[*16*] Pinnington, R. J., and Briscoe, A. R., "A Wave Model for a Pneumatic Tyre Belt," *Journal of Sound and Vibration*, Vol. 252, 2002, pp. 941–959.

[*17*] Kim, B. S., Kim, G. J., and Lee, T. K., "The Identification of Sound Generating Mechanisms of Tyres," *Applied Acoustics*, Vol. 68, 2007, pp. 114–133.

[*18*] Perisse, J., Clariet, J. M., and Hamet, J. F., "Modal Testing of a Smooth Tire in Low and Medium Frequency-Estimation of Structural Parameters," SPIE Conferences and Exhibitions, San Antonio, TX, 2000.

[*19*] McBride, S., Burdisso, R., and Sandu, C., "A Comparison between Modal and Wave Propagation Models for Simulation of Tire-Pavement Interaction Noise," *INTER-NOISE and NOISE-CON Congress and Conference Proceedings*, Vol. 258, 2018, pp. 1335–1344.

[*20*] Liu, F., Sutcliffe, M. P. F., and Graham, W. R., "Modeling of Tread Block Contact Mechanics Using Linear Viscoelastic Theory," *Tire Science and Technology*, Vol. 36, 2008, pp. 211–226.

[*21*] Liu, F., Sutcliffe, M. P. F., and Graham, W. R., "Prediction of Tread Block Forces for a Free-Rolling Tyre in Contact with a Smooth Road," *Wear*, Vol. 269, 2010, pp. 672–683.

[*22*] Lopez Arteaga, I., "Tyre/Road Noise and Vibration: Understanding Their Interaction and Contribution to Vehicle Noise and Fuel Consumption," 21st International Congress on Sound and Vibration (ICSV 21), Beijing, China, 2014.

[*23*] Hofstetter, K., Grohs, Ch., Eberhardsteiner, J., and Mang, H. A., "Sliding Behaviour of Simplified Tire Tread Patterns Investigated by Means of FEM," *Computers & Structures*, Vol. 84, 2006, pp. 1151–1163.

[*24*] Wu, T. W., *Boundary Element Acoustics: Fundamentals and Computer Codes*, WIT Press, Southampton, UK, 2000.

[*25*] AASHTO, *TP-76: Standard Method of Test for Measurement of Tire/Pavement Noise Using the On-Board Sound Intensity (OBSI) Method*, 2015.